TU Delft

Delft University of Technology

Document Version
Final published version

Licence
Dutch Copyright Act (Article 25fa)

Citation (APA)
Deng, Z., Zhang, S., Zhu, G., Dong, J., & Bauer, P. (2026). Direct Matrix Converter-Based Modular High-Power Wireless Charging Systems for Heavy-Duty Electric Vehicles. *IEEE Journal on Wireless Power Technologies*, *1*. https://doi.org/10.1109/JWPT.2026.3670766

Important note
To cite this publication, please use the final published version (if applicable).
Please check the document version above.

Copyright
In case the licence states “Dutch Copyright Act (Article 25fa)”, this publication was made available Green Open Access via the TU Delft Institutional Repository pursuant to Dutch Copyright Act (Article 25fa, the Taverne amendment). This provision does not affect copyright ownership.
Unless copyright is transferred by contract or statute, it remains with the copyright holder.

Sharing and reuse
Other than for strictly personal use, it is not permitted to download, forward or distribute the text or part of it, without the consent of the author(s) and/or copyright holder(s), unless the work is under an open content license such as Creative Commons.

Takedown policy
Please contact us and provide details if you believe this document breaches copyrights.
We will remove access to the work immediately and investigate your claim.

This work is downloaded from Delft University of Technology.

Direct Matrix Converter-Based Modular High-Power Wireless Charging Systems for Heavy-Duty Electric Vehicles

Zichen Deng, *Graduate Student Member, IEEE*, Shibo Zhang, *Graduate Student Member, IEEE*, Gangwei Zhu, *Member, IEEE*, Jianning Dong, *Senior Member, IEEE*, and Pavol Bauer, *Senior Member, IEEE*

***Abstract*—Due to the increasing demand for high-power charging in heavy-duty electric vehicles (HDEVs) and the inherent limitations of conductive charging, the development of a modular wireless power transfer (WPT) charging system has become indispensable. However, most existing studies rely on conventional two-stage AC-DC-AC converters at the primary side, which limit power density and reliability because of the bulky DC-link electrolytic capacitors. This paper proposes a novel modular medium-voltage AC (MVAC) grid-connected WPT system based on direct matrix converters (DMCs). A full-bridge DMC (FBDMC)-based WPT system is proposed with a simple fixed 50 % duty-cycle modulation strategy. Analytical and simulation results verify that the AC-input FBDMC-based WPT system can be equivalently represented by a DC-input full-bridge inverter-based WPT system with the same series-series compensation, RMS input voltage, and modulation. To achieve higher power transfer capability, scalability, and efficiency, input-series output-parallel (ISOP) and input-parallel output-series (IPOS) modular topologies are investigated. The simulation results demonstrate that, when connected to the MVAC grid using the ISOP configuration, the system is capable of delivering power at the hundred-kW to MW level. The proposed topologies are verified by the downscaled experimental platform. The FBDMC-based prototype achieves an output power of 2.51 kW with a grid-to-load efficiency of 91.6 % at 230 VAC. The IPOS and ISOP configurations are experimentally validated using two modular half-bridge DMC (HBDMC) modules derived from the FBDMC design.**

***Index Terms*—Direct matrix converter (DMC), single-stage AC-AC conversion, modular structure, wireless power transfer (WPT).**

NOMENCLATURE

f_s	Switching frequency.
ω_s	Angular switching frequency.
T_s	Switching period.
L_p	Primary self-inductance of the charging coil.
C_p	Primary compensation capacitor in a series-series (SS)-compensated WPT system.
L_s	Secondary self-inductance of the charging coil.
C_s	Secondary compensation capacitor in a SS-compensated WPT system.
R_L	Load resistance.
V_p	RMS value of the fundamental component of the primary-side port (P_a–P_b) voltage of the SS-compensated WPT system.
I_p	RMS value of the fundamental component of the primary coil current in the SS-compensated WPT system.
R_p	Equivalent resistance of the primary resonant network.
V_s	RMS value of the fundamental component of the secondary-side port (S_a–S_b) voltage of the SS-compensated WPT system.
I_s	RMS value of the fundamental component of the secondary coil current in the SS-compensated WPT system.
R_s	Equivalent resistance of the secondary resonant network.
M	Mutual inductance between the primary and secondary coils.
R_{AC}	Equivalent AC load of R_L reflected to the AC side through the secondary-side rectifier and DC capacitor filter.
$v_{p,DC}(t)$	Instantaneous bipolar square-wave voltage applied to the primary-side port of the DC-input full-bridge inverter-based SS-compensated WPT system.
V_{DC}	Amplitude of the input DC voltage.
$s_{sw}(t)$	Bipolar switching function of the full-bridge inverter or the full-bridge direct matrix converter (FBDMC) output voltage.
$V_{p,DC,FHA}$	RMS value of the fundamental component of $v_{p,DC}(t)$.
$v_{p,AC}(t)$	Instantaneous bipolar square-wave voltage applied to the primary-side port of the AC-input FBDMC-based SS-compensated WPT system.
$V_{grid,rms}$	RMS value of the input AC grid voltage.
ω_g	Angular grid frequency.
T_g	Grid period.
$v_{p,AC,FHA,s}(t)$	RMS value of the switching-frequency fundamental component of $v_{p,AC}(t)$, which varies with the grid frequency.
$V_{p,AC,FHA,g}$	RMS value of $v_{p,AC,FHA,s}(t)$ evaluated over one grid period.
$R_{AC,dc}$	R_{AC} of the DC-input full-bridge inverter-based SS-compensated WPT system.

Received 7 November 2025; revised 29 January 2026; accepted 25 February 2026. Date of publication 5 March 2026; date of current version 27 March 2026. The associate editor coordinating the review of this article and approving it for publication was Dr. Alessandra Costanzo. *(Corresponding author: Jianning Dong.)*

Zichen Deng, Shibo Zhang, Jianning Dong, and Pavol Bauer are with the DC System, Energy Conversion and Storage (DCE&S) Group, Faculty of Electrical Engineering, Mathematics and Computer Science (EEMCS), Delft University of Technology, 2624 CP Delft, The Netherlands (e-mail: z.deng-4@tudelft.nl; s.zhang-6@tudelft.nl; j.dong-4@tudelft.nl; p.bauer@tudelft.nl).

Gangwei Zhu is with the Department of Electrical Engineering, City University of Hong Kong, Kowloon, Hong Kong (e-mail: gangwzhu@cityu.edu.hk).

Digital Object Identifier 10.1109/JWPT.2026.3670766

3066-2494 © 2026 IEEE. All rights reserved, including rights for text and data mining, and training of artificial intelligence and similar technologies. Personal use is permitted, but republication/redistribution requires IEEE permission. See https://www.ieee.org/publications/rights/index.html for more information.

Authorized licensed use limited to: TU Delft Library. Downloaded on October 06,2026 at 11:01:11 UTC from IEEE Xplore. Restrictions apply.

$i_{ac}(t)$	Switching-frequency fundamental component of AC current at the input of the rectifier of the AC-input FBDMC-based SS-compensated WPT system.
$I_{env}(t)$	Envelope amplitude of the switching-frequency fundamental component of $i_{ac}(t)$, which varies with the grid frequency.
$I_{AC,rms,g}$	RMS value of the current envelope $I_{env}(t)$ evaluated over one grid period.
C_{dc}	DC-link filter capacitor at the output of the rectifier.
$i_o(t)$	Output current through R_L.
$R_{AC,ac}$	R_{AC} of the AC-input FBDMC-based SS-compensated WPT system.
$\overline{P}_{ac}$	Active power delivered to R_{AC}.
$\overline{P}_{load}$	Active power delivered to R_L.
U_{out}	Output voltage on R_L in the input-parallel-output-series configuration.
P_{out}	Output active power delivered to R_L.
n	Number of modules in the proposed modular configurations.
$I_{in,grid}$	Grid-side input current.
U_i	Input voltage of a single module.
$I_{in,mod}$	Input current of a single module.

I. Introduction

Heavy-duty vehicles (HDVs) are responsible for more than a quarter of greenhouse gas (GHG) emissions from road transport in the European Union (EU) and account for over 6 % of the total EU GHG emissions [1]. Considering the emission standards for HDVs in the EU [2] and the indispensable role of HDVs in freight and industrial transportation, electrifying HDVs is of great significance.

Several heavy-duty electric vehicle (HDEV) models have been introduced to the market [3], [4]. However, charging power remains one of the major bottlenecks hindering large-scale deployment compared with fossil fuel-based HDVs. In contrast to the conductive charging approach, which suffers from challenges such as bulky cables and limited user convenience, wireless power transfer (WPT) technology has emerged as a more user-friendly alternative, offering weatherproof, hands-free, safe, and fully autonomous charging solutions for electric vehicles. A typical WPT system configuration is illustrated in Fig. 1.

For HDEVs to compete with conventional HDVs, the charging power must reach the MW level, making a modular system design indispensable. Kim et al. developed an 818-kW modular WPT system for the dynamic charging of trains [5]. In addition, novel transformerless multilevel WPT topologies have been proposed in [6], [7], [8] to further improve the power density, MV-level insulation, and fail-safe properties. Other researchers have demonstrated WPT systems exceeding 1 MW for electric ships by employing modular H-bridge converters and large rectangular coil pairs [9]. Nevertheless, the operating frequency of such systems is constrained to 2–8 kHz because of the use of IGBTs. The cascaded H-bridge (CHB) converter and its variants have also been extensively investigated for WPT applications [10], [11], [12], [13]. Furthermore, the use of modular multilevel converters (MMCs) as the primary power converter in WPT systems has been explored in several studies [14], [15], [16], [17], [18], [19]. To further enhance current transfer capability and system scalability, parallel connection of inverters and rectifiers has also been investigated by multiple researchers [20], [21], [22], [23], [24], [25], [26], [27], [28].

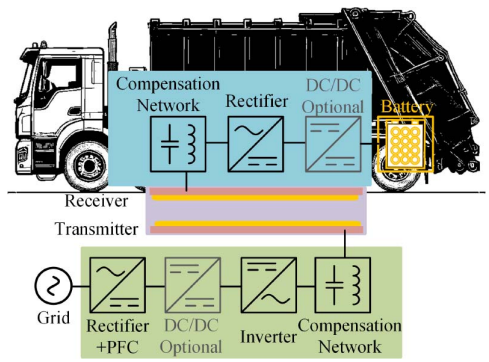


Fig. 1. Typical WPT system.

However, several challenges remain in the existing research. Most studies have focused on the conventional two-stage primary power conversion topology, which refers to an AC-DC rectifier stage followed by a DC-AC H-bridge stage with an intermediate stiff DC-link capacitor that relies heavily on bulky electrolytic capacitors. These capacitors not only reduce overall system efficiency [29], but also deteriorate power density and long-term reliability. Only a limited number of studies have investigated grid-connected, direct AC-AC converter-based WPT systems [30], [31], [32], [33], [34], [35], [36], [37], [38]. However, none of these works have explored the potential of modularity within direct AC-AC converter-based WPT topology for high-power charging applications.

Based on the above discussion, this paper proposes a novel medium-voltage AC (MVAC) grid-connected, direct matrix converters (DMCs)-based modular system to enhance the power transfer capability, power density, flexibility, and modularity of wireless power transfer (WPT) charging systems. Modular DMCs are employed as the grid interface between the MVAC grid and the transmitter coils. Furthermore, several novel connections between the primary converter and charging coil have been proposed to increase the power transfer capability and modularity of the WPT charging systems.

This article is structured as follows. Section II introduces the proposed modular WPT system. First, the single full-bridge direct matrix converter (FBDMC)-based single-phase WPT system is presented. The circuit model is established and analyzed. Then, the FBDMC-based WPT systems adopting both IPOS and ISOP configurations are proposed. Section III provides simulation results to verify the feasibility of the proposed topologies. Section IV presents the experimental platform and corresponding results. Finally, Section V concludes the paper.

II. Proposed Modular System

A. Single FBDMC-Based Single-Phase WPT System

Fig. 2 illustrates the circuit topology of the proposed single FBDMC-based single-phase WPT system. The FBDMC also serves as a fundamental building cell for the modular configurations discussed in the subsequent subsections and for the simulation studies.

Authorized licensed use limited to: TU Delft Library. Downloaded on October 06,2026 at 11:01:11 UTC from IEEE Xplore. Restrictions apply.

To provide an intuitive comparison between the conventional two-stage primary power conversion and the proposed FBDMC-based single-stage primary power conversion, the grid line-to-line RMS voltage, load current, and ripple are assumed to be 800 V, 25 A, and 1 %, respectively. Under these conditions, the required DC-link filter capacitance for a three-phase two-stage converter is approximately 5 mF. Considering the voltage and capacitance limitations of commercial electrolytic capacitors, multiple capacitors must be connected in both series and parallel. For example, 4700 μF/550 V electrolytic capacitors are employed, and the DC output voltage of the three-phase rectifier is approximately 1080 V. To achieve a 1650-V voltage rating, 3 capacitors are connected in series. Furthermore, to obtain an equivalent capacitance of 4.7 mF, 3 such series groups are connected in parallel. Consequently, a total of 9 capacitors are required. Based on dimensions in datasheet [39], the total volume of the DC-link capacitors is about 12400 cm^3, excluding the additional requirements for heat dissipation and mechanical layout. This bulky DC-link is eliminated in the proposed topology, leading to a significantly higher power density for the FBDMC-based single-stage WPT system.

Compared with the half-bridge and T-type DMCs, the FBDMC offers the highest control flexibility, as well as the lowest current stress and conduction loss, as reported in [40]. Nevertheless, the other two configurations also exhibit certain advantages. For instance, when system cost is the primary concern, the half-bridge DMC becomes a more favorable choice.

Four pairs of common-source back-to-back MOSFETs are exployed as four-quadrant switches to convert the low-frequency AC (LFAC) voltage to high-frequency AC (HFAC) voltage. The series-series (SS) compensation topology is used here for illustration, while other compensation methods, such as dual-side LCC (DLCC), can also be adopted. On the secondary side, either a diode-based rectifier can be utilized to form the simplest system, or an active rectifier can be employed to enhance efficiency, increase control flexibility, and enable bidirectional power flow for vehicle-to-grid (V2G) or vehicle-to-everything (V2X) applications.

In this paper, a simple open-loop fixed-duty modulation scheme with a 50 % duty cycle is adopted, where a small dead time is inserted in practical implementation.

The equivalent circuit model of the FBDMC-based SS-compensated WPT system, derived from the port pairs P_a–P_b and S_a–S_b in Fig. 2, is shown in Fig. 3. Based on this model, the analytical equivalence between the AC-input FBDMC-based WPT system with SS compensation (referred to as the AC-FBDMC-SS WPT system) and the DC-input full-bridge inverter-based WPT system with SS compensation (referred to as the DC-FBI-SS WPT system) is derived using first-harmonic analysis (FHA) as follows.

Based on the symbols defined in the Nomenclature, the resonance conditions can be expressed as

$$\begin{cases} \omega_s^2 L_p C_p = 1 \\ \omega_s^2 L_s C_s = 1 \end{cases} \tag{1}$$

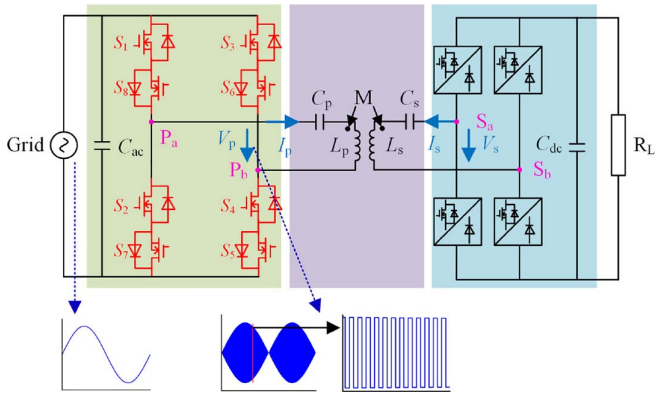


Fig. 2. Proposed FBDMC-based single-phase single-stage WPT system with series-series (SS) compensation.

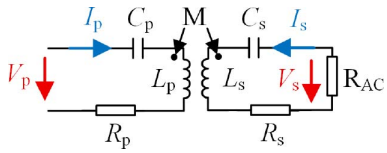


Fig. 3. The equivalent circuit model of the AC-FBDMC-SS WPT system seen from the ports P_a–P_b and S_a–S_b of Fig. 2.

Then, by applying Kirchhoff's voltage law (KVL), the following equations can be obtained

$$\begin{cases} V_p = R_p I_p + j\omega_s M I_s \\ 0 = (R_s + R_{AC}) I_s + j\omega_s M I_p \end{cases} \tag{2}$$

By solving (2), the current I_p, I_s, and the voltage V_s can be expressed as

$$|I_p| = \frac{|V_p|}{R_p + \dfrac{(\omega_s M)^2}{R_s + R_{AC}}} \tag{3}$$

$$|I_s| = \frac{\omega_s M}{R_s + R_{AC}} \cdot \frac{|V_p|}{R_p + \dfrac{(\omega_s M)^2}{R_s + R_{AC}}} \tag{4}$$

$$|V_s| = |I_s| R_{AC} \tag{5}$$

Therefore, the output power can be expressed as,

$$P_o = |I_s|^2 R_{AC} = K |V_p|^2 \tag{6}$$

where

$$K = \left(\frac{(\omega_s M)^2}{(R_s + R_{AC})^2} \cdot \frac{R_{AC}}{\left(R_p + \frac{(\omega_s M)^2}{R_s + R_{AC}} \right)^2} \right) \tag{7}$$

From the above equations, it can be observed that for WPT systems with identical coil parameters, the output performances are only determined by V_p and R_{AC}.

1) V_p: For a DC-FBI-SS system,

$$\begin{cases} v_{p,DC}(t) = V_{DC} \cdot s_{sw}(t) \\ s_{sw}(t) \in \{-1, +1\}, \text{ switching at } f_s \end{cases} \tag{8}$$

Authorized licensed use limited to: TU Delft Library. Downloaded on October 06,2026 at 11:01:11 UTC from IEEE Xplore. Restrictions apply.

For a full-bridge bipolar square-wave output voltage with a duty cycle of 50 %, the RMS value of its fundamental component, obtained from Fourier series expansion, can be expressed as follows.

$$V_{\mathrm{p,DC,FHA}} = \frac{4}{\pi\sqrt{2}} V_{\mathrm{DC}} \tag{9}$$

In contrast, for the AC-FBDMC-SS WPT system, the grid voltage varies in amplitude at grid frequency (50 Hz in Europe), whereas the operating frequency of the FBDMC is approximately 85 kHz, which is much higher than the grid frequency. Therefore, the amplitude of the input voltage of the primary compensation network can be regarded as constant within a single switching period (approximately 11.76 μs), while varying over the grid period (20 ms for a 50-Hz grid). Thus,

$$\begin{cases} v_{\mathrm{p,AC}}(t) = \sqrt{2} V_{\mathrm{grid,rms}} |\sin(\omega_{\mathrm{g}} t)| \cdot s_{\mathrm{sw}}(t) \\ s_{\mathrm{sw}}(t) \in \{-1, +1\}, \text{ switching at } f_{\mathrm{s}} \end{cases} \tag{10}$$

In this paper, the duty cycle of MOSFETs is also 50 %. Therefore, the RMS value of the fundamental component at the switching frequency is

$$v_{\mathrm{p,AC,FHA,s}}(t) = \frac{4}{\pi\sqrt{2}} \sqrt{2} V_{\mathrm{grid,rms}} |\sin(\omega_{\mathrm{g}} t)| \tag{11}$$

which varies with the grid period. Accordingly, the RMS value of the fundamental component at the grid frequency can be expressed as follows.

$$\begin{aligned} V_{\mathrm{p,AC,FHA,g}} &= \sqrt{\frac{1}{T_g} \int_0^{T_g} v_{\mathrm{p,AC,FHA,s}}^2(t)\ \mathrm{d}t} \\ &= \frac{4}{\pi\sqrt{2}}\ V_{\mathrm{grid,rms}} \end{aligned} \tag{12}$$

Therefore, from (9) and (12), it can be observed that the V_{p} of the DC-FBI-SS WPT system is equal to that of the AC-FBDMC-SS WPT system when the input DC voltage equals the RMS value of the input AC voltage, as given in (13).

$$\begin{cases} V_{\mathrm{DC}} = V_{\mathrm{grid,rms}} \\ V_{\mathrm{p,DC,FHA}} = V_{\mathrm{p,AC,FHA,g}} \end{cases} \tag{13}$$

2) R_{AC}: For a DC-FBI-SS WPT system with a passive diode-based full-bridge rectifier and a DC capacitor filter, the relationship between R_{AC} and R_{L} can be expressed as [41]

$$R_{\mathrm{AC,dc}} = \frac{8}{\pi^2} R_{\mathrm{L}} \tag{14}$$

For the AC-FBDMC-SS WPT system that shares the same secondary configuration as the DC-FBI-SS WPT system, under FHA, the fundamental component of the rectifier input current at the switching frequency can be expressed as

$$\begin{cases} i_{\mathrm{ac}}(t) = I_{\mathrm{env}}(t) \sin(\omega_{\mathrm{s}} t) \\ I_{\mathrm{env}}(t) = \sqrt{2} I_{\mathrm{AC,rms,g}} |\sin(\omega_{\mathrm{g}} t)| \end{cases} \tag{15}$$

After rectification, a small DC-side capacitor is employed to attenuate the switching-frequency ripple components. Considering the time-scale separation $T_{\mathrm{s}} \ll R_{\mathrm{L}} C_{\mathrm{dc}} \ll T_{\mathrm{g}}$, a slowly varying output DC current with a double-grid-frequency ripple component is obtained, resulting in a pulsed charging behavior that has been reported to be acceptable for battery charging applications [42]. Considering that the double-grid-frequency envelope component can be regarded as quasi-constant within one switching period, the output current can be expressed as

$$\begin{aligned} i_{\mathrm{o}}(t) &\approx \frac{1}{T_s} \int_t^{t+T_s} |I_{\mathrm{env}}(t) \sin(\omega_s \tau)| d\tau \\ &= \frac{2}{\pi}\ |I_{\mathrm{env}}(t)| \end{aligned} \tag{16}$$

Assuming that the power losses of the rectifier and the capacitors are negligible, the equivalent impedances of the AC link and DC link can be derived by equating the average transferred power over one grid period.

The average active power observed from the AC side and delivered to the DC load over one grid period can be expressed as

$$\overline{P}_{\mathrm{ac}} = \frac{1}{T_{\mathrm{g}}} \int_{t_0}^{t_0+T_{\mathrm{g}}} i_{\mathrm{ac}}^2(t)\ R_{\mathrm{AC,ac}}\ \mathrm{d}t \tag{17}$$

$$\overline{P}_{\mathrm{load}} = \frac{1}{T_{\mathrm{g}}} \int_{t_0}^{t_0+T_{\mathrm{g}}} i_{\mathrm{o}}^2(t)\ R_{\mathrm{L}}\ \mathrm{d}t \tag{18}$$

Substituting (15) into (17) and (16) into (18) yields

$$\overline{P}_{\mathrm{ac}} = \frac{R_{\mathrm{AC,ac}}}{2T_{\mathrm{g}}} \int_{t_0}^{t_0+T_{\mathrm{g}}} I_{\mathrm{env}}^2(t)\ \mathrm{d}t \tag{19}$$

$$\overline{P}_{\mathrm{load}} = \frac{4R_{\mathrm{L}}}{\pi^2 T_{\mathrm{g}}} \int_{t_0}^{t_0+T_{\mathrm{g}}} I_{\mathrm{env}}^2(t)\ \mathrm{d}t \tag{20}$$

Equating (19) and (20) gives the AC-side resistive load seen by the resonant link:

$$R_{\mathrm{AC,ac}} = \frac{8}{\pi^2}\ R_L. \tag{21}$$

As a result, $R_{\mathrm{AC,dc}} = R_{\mathrm{AC,ac}}$.

Based on the above analytical derivations, it can be concluded that, under identical coil parameters, SS compensation network, and the fixed 50 % duty-cycle modulation scheme, the AC-FBDMC-SS WPT system and the DC-FBI-SS WPT system exhibit identical V_{p}, V_{s}, I_{p}, I_{s}, and P_{o} when their input voltage RMS values are equal. This equivalence is established through the first-harmonic modeling and time-scale separation analysis. As a result, the AC-FBDMC-SS WPT system can be analyzed and designed using the well-established optimization framework of the DC-FBI-SS WPT systems [43], [44].

B. Multiple DMC-Based Single-Phase WPT System

1) Input-Parallel-Output-Series (IPOS): According to [43], the most losses in the magnetic link of the WPT system are proportional to the square of the coil current. Consequently, for an identical power level, a lower current leads to higher efficiency.

Therefore, WPT coils operating at higher voltage levels possess greater practical value for high-power applications. This principle is applicable not only to HDEVs but also to low-duty

Authorized licensed use limited to: TU Delft Library. Downloaded on October 06,2026 at 11:01:11 UTC from IEEE Xplore. Restrictions apply.

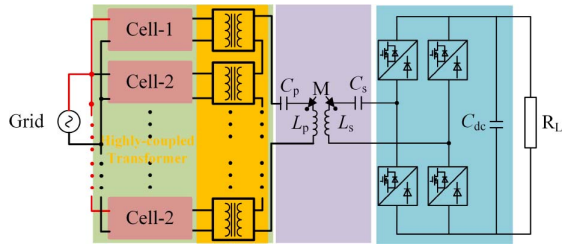


Fig. 4. Single-phase FBDMC-based IPOS WPT system.

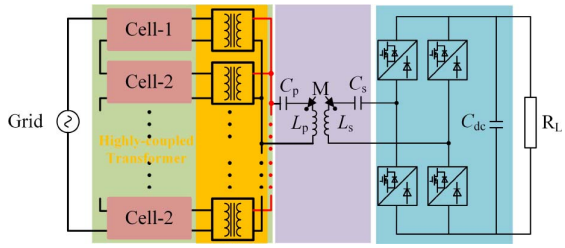


Fig. 5. Single-phase DMC-based ISOP WPT system.

electric vehicles (LDEVs). For instance, in the case of residential charging for LDEVs supplied from a standard 230-V grid at home, it is challenging for a conventional front-end converter to generate an 85-kHz, 800-V voltage required for high-efficiency charging. This limitation leads to energy loss and increased operating costs. To overcome this issue, a modular IPOS structure has been proposed, as illustrated in Fig. 4, where each cell represents the same FBDMC as shown in Fig. 2. In this configuration, highly coupled transformers are employed to connect the outputs of the FBDMCs in series. This structure enables the realization of higher voltage levels under limited grid-voltage conditions, thereby enhancing the power transfer capability and the overall charging efficiency.

2) Input-Series-Output-Parallel (ISOP): Although the IPOS structure can achieve high-voltage wireless power transfer (WPT) under a low-voltage grid, the capacity of the low-voltage grid is insufficient to supply high power. For example, a typical residential three-phase connection of 3 × 230 V × 25 A can provide a maximum power of approximately 17.25 kW. Considering that the ultimate goal for a single HDEV charging spot is to achieve MW-level charging power, a medium-voltage (MV) grid connection becomes necessary.

A DC grid could, in principle, deliver high power efficiently; however, most DC charging infrastructures are converted from AC grids, except in the case of sustainable energy sources such as photovoltaic systems. Thus, converter stations and bulky DC-link capacitors are still required for a DC grid. Consequently, it is more practical to develop an MVAC grid interface that directly converts LFAC voltage into HFAC for WPT applications.

Nevertheless, due to the voltage ratings of the most advanced SiC and GaN MOSFETs, a cascaded converter structure is necessary to interface with the MVAC grid. However, the voltage applied to the coil cannot be increased without limitation. It is much easier to design high-input-current coils by paralleling Litz wires than to design ultra-high-input-voltage coils, primarily due to insulation challenges. According to [43], in SS-compensated WPT systems with optimized coil design and a high figure-of-merit (FOM = kQ) given by the product of the magnetic coupling k and the quality factor Q of the charging pads, the voltage across the compensation capacitors can be significantly higher than the input DC voltage. Due to the series resonance, the voltage amplitude across the coils is similar to that across the capacitors. Therefore, although ultra-high-input-voltage coils can theoretically achieve higher efficiency, they are difficult to implement in practice. In addition, the secondary side of the ultra-high-voltage coil still requires a step-down converter to match the battery voltage.

TABLE I
PARAMETERS OF THE COMPONENTS IN SIMULATIONS

Variables	Symbols	Value	Units
Grid Voltage RMS value	U_{grid} (RMS)	800	V
Grid frequency	f_{grid}	50	Hz
Switching frequency	f_{sw}	87	kHz
Primary inductance	L_p	71.6	μH
Primary-side capacitor	C_p	48.965	nF
Secondary inductance	L_s	71.6	μH
Secondary-side capacitor	C_s	48.965	nF
Mutual inductance	M	16.5	μH
Load resistance	R_L	10.8716	Ω
Grid-side capacitor	C_{ac}	10	μ F
Load-side capacitor	C_{dc}	10	μ F

Therefore, the ISOP structure is adopted in this work. Similar to the configuration of a cascaded H-bridge converter, multiple cascaded cells are employed to form a high-voltage grid interface capable of extracting MW-level power from the MVAC grid. The proposed cascaded FBDMC-based WPT system is illustrated in Fig. 5, where each cell represents the same FBDMC as shown in Fig. 2.

As shown in Fig. 5, additional highly coupled transformers are employed to achieve the parallel output connection of each cell. This ISOP structure is one of the most commonly used modular configurations in the MV grid-tied converters. Although these extra transformers are introduced, their impact on overall efficiency is minimal, as the efficiency of high-frequency transformers can easily reach approximately 99 % [45].

III. Simulation Results

A. Single FBDMC-Based Single-Phase WPT System

The simulation parameters of the rectangular coils are based on [46]. The detailed system parameters are listed in Table I. The ideal semiconductor switches and idealized resonant components are adopted in the simulation, because the following results are used to validate the analytical equivalence derived in Section II-A, and to demonstrate the functional behavior of the single FBDMC and scalability characteristics of the proposed IPOS and ISOP topologies at the topology level, rather than to perform a detailed loss analysis, efficiency optimization, or device-level performance comparison.

All simulations are carried out in PLECS using a fixed-step discrete solver. The simulation time step is set to 10 ns to accurately capture the high-frequency switching dynamics at the switching frequency. The total simulation duration is 30 ms, and

Authorized licensed use limited to: TU Delft Library. Downloaded on October 06,2026 at 11:01:11 UTC from IEEE Xplore. Restrictions apply.

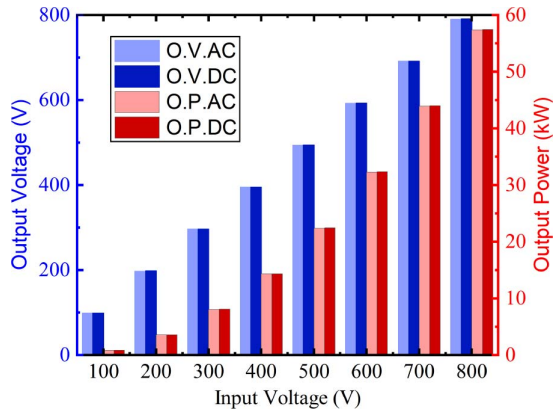


Fig. 6. Comparisons of output performance between the AC-FBDMC-SS WPT system and the DC-FBI-SS WPT system. O.V.AC means the output voltage of the AC system. O.V.DC means the output voltage of the DC system. O.P.AC means the output power of the AC system. O.P.DC means the output power of the DC system.

TABLE II
THE OUTPUT PERFORMANCES OF IPOS CONFIGURATION. O.V. MEANS THE OUTPUT VOLTAGE. O.P. MEANS THE OUTPUT POWER

No. of Modules	O.V. (V)	O.P. (kW)
1	231	4.9
2	463	19.7
3	694	44.3
4	925	78.7

all RMS values reported in this paper are evaluated over the steady-state interval from 10 ms to 30 ms to avoid transient effects. The dead time was set to 0 in all simulations to avoid introducing modulation-dependent distortion effects and to improve simulation efficiency.

A comparative simulation study is conducted between the AC-FBDMC-SS WPT system and the DC-FBI-SS WPT system under identical system configurations to verify both the correctness of the analytical equivalence derived in Section II-A and the feasibility of the proposed AC-FBDMC-SS WPT system. The DC input voltage of the DC-FBI-SS WPT system is selected according to the analytical equivalence condition in (13). The simulation results are shown in Fig. 6.

As shown in Fig. 6, the difference in output power between the two systems is below 0.15 %. This close agreement confirms the correctness of the analytical derivations in Section II-A and verifies the feasibility of the proposed AC-FBDMC-SS WPT system.

B. Multiple FBDMC-Based Single-Phase WPT System

1) IPOS: The proposed topology is designed to address the issue of insufficient input grid voltage, which limits the effective excitation of high-voltage WPT coils and degrades overall system performance. In the simulation, the input voltage was set to 230 V in accordance with the European residential grid standard, while all other system parameters were identical to those specified in Section III-A. The impact of employing different numbers of modules (i.e., 1, 2, 3, and 4) on the output performance was investigated through simulations, and the results are summarized in Table II.

TABLE III
THE RELATIONSHIP BETWEEN OUTPUT PERFORMANCES AND THE NUMBER OF MODULES. U_i AND I_i ARE THE INPUT VOLTAGE AND INPUT CURRENT OF ONE SINGLE MODULE, RESPECTIVELY. U_o, I_o, AND P_o ARE THE OUTPUT VOLTAGE, OUTPUT CURRENT, AND OUTPUT POWER OF ONE SINGLE MODULE. I.V. MEANS THE INPUT VOLTAGE. I.C. MEANS THE INPUT CURRENT. O.V. MEANS THE OUTPUT VOLTAGE. O.C. MEANS THE OUTPUT CURRENT. O.P. MEANS THE OUTPUT POWER

No. of Modules	I.V.	I.C.	O.V.	O.C.	O.P.
1	U_i	I_i	U_o	I_o	P_o
2	U_i	$4I_i$	$2U_o$	$2I_o$	$4P_o$
n	U_i	n^2I_i	nU_o	nI_o	n^2P_o

It can be demonstrated and summarized that the following patterns exist.

As shown in Table III, in the IPOS configuration system, the input voltage remains constant due to the input-parallel connection, while the series-connected output leads to the output voltage being linearly proportional to the number of modules n,

$$U_{\text{out}} \propto n \tag{22}$$

With a fixed load resistance, the output power exhibits a quadratic relationship with the number of modules n

$$P_{\text{out}} = \frac{U_{\text{out}}^2}{R_{\text{L}}} \propto n^2 \tag{23}$$

By power balance (neglecting losses), the total grid input current therefore scales as

$$I_{\text{in,grid}} \approx \frac{P_{\text{out}}}{U_{\text{i}}} \propto n^2 \tag{24}$$

As a result, due to the input-parallel connection and n modules, the input current of each module is linearly proportional to the number of modules n

$$I_{\text{in,mod}} \propto n \tag{25}$$

It should be noted that the maximum transmission efficiency of the wireless charging coil depends on the angular frequency ω_s, the mutual inductance M, and the equivalent load R_{AC} as indicated in [44]. For a given coil, the optimal load R_{L} corresponding to the maximum transfer efficiency is fixed. Therefore, if insulation limitations are neglected, increasing the input voltage can further enhance the transferred power. Nevertheless, both the current drawn from the single-phase grid and the current flowing through each converter increase accordingly, leading to higher conduction losses and instability in the grid. As a result, the IPOS structure is best suited for medium-power (below 20 kW) applications with low input voltage, such as the residential grid.

2) ISOP: The proposed topology is designed to address the challenge of directly interfacing high-power wireless charging systems with the MVAC grid. At high-power levels ($>$ 20 kW according to SAE J2954/2 [47]), the voltage and power ratings of currently available MOSFETs limit the capability of a single converter, making it insufficient to meet system requirements. Therefore, the ISOP structure is adopted. In the simulation, a two-module and a three-module cascaded structure connected to 1.6-kV and 2.4-kV AC grids, respectively, are compared with a

Authorized licensed use limited to: TU Delft Library. Downloaded on October 06,2026 at 11:01:11 UTC from IEEE Xplore. Restrictions apply.

TABLE IV
THE COMPARISON BETWEEN DIFFERENT GRID VOLTAGES AND MODULES AT THE SAME LOAD CONDITION. I.V. MEANS THE INPUT VOLTAGE. M.C. MEANS THE CURRENT OF EACH SINGLE MODULE. O.P. MEANS THE OUTPUT POWER

No. of Modules	I.V. (V)	M.C. (A)	O.P. (kW)
1	800	84	59.6
2	1600	42	59.6
3	2400	28	59.6
4	$n\times$800 V	84/n	59.6

TABLE V
THE COMPARISON BETWEEN DIFFERENT GRID VOLTAGES AND MODULES AT THE SAME INPUT CURRENT. I.V. MEANS INPUT VOLTAGE. M.C. MEANS THE CURRENT OF EACH SINGLE MODULE. O.P. MEANS THE OUTPUT POWER

No. of Modules	I.V. (V)	M.C. (A)	O.P. (kW)
1	800	84	59.6
2	1600	84.6	118.7
3	2400	85.1	177.2
4	$n\times$800 V	84	$n\times$59.6

single module connected to an 800-V grid. Two simulation cases are conducted.

In the first case, the coil parameters and load are kept identical for both configurations, resulting in the same output power, and the input currents are compared. The results are summarized in Table IV.

As shown in Table IV, increasing the input voltage and employing more cascaded modules reduces the module current, which is also the grid current. Therefore, under identical load conditions, the current stress on both the grid and the semiconductor switches is further alleviated, leading to higher efficiency due to reduced conduction losses.

In the second case, the coil and load parameters are adjusted for the two- and three-module cascaded configurations, respectively, so that each module operates with the same input voltage and current, and the resulting output powers are compared in Table V.

It is clear that, under the same input current condition, where each module delivers its rated power, the output power is linearly proportional to the number of modules n,

$$P_{\text{out}} \propto n \tag{26}$$

while each module maintain the same input voltage and current. By employing the ISOP structure, the output power can be significantly increased while maintaining the same stress on each semiconductor switch. This structure greatly increases the power transfer capability, scalability, and flexibility of the WPT system.

IV. EXPERIMENT RESULTS

Due to laboratory safety and the output voltage limit of the AC power supply Grid Emulator GE-40 kVA vAC/DC from Cinergia, a downscaled prototype is implemented to experimentally verify the proposed topology.

The proposed topology is experimentally validated using the developed prototype shown in Fig. 7, which represents an AC-

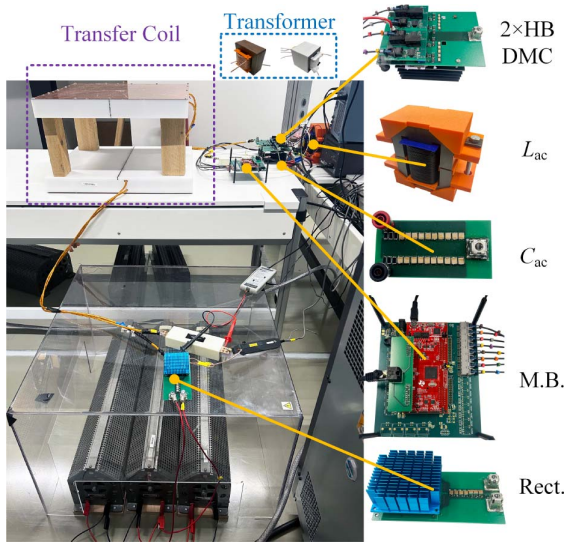


Fig. 7. Experimental platform. M.B. represents the modulation board. Rect. represents the rectifier.

TABLE VI
PARAMETERS OF THE EXPERIMENTAL COMPONENTS

Variables	Symbols	Value	Units
Grid Voltage RMS value	U_{grid}	230	V
Grid filter inductor	L_{ac}	1.1	mH
Switching frequency	f_{sw}	86.2	kHz
Primary inductance	L_{p}	292.3	μH
Primary-side capacitor	C_{p}	11.99	nF
Secondary inductance	L_{s}	199.6	μH
Secondary-side capacitor	C_{s}	17.57	nF
Mutual inductance	M	23.375	μH
Load resistance	R_{L}	15.5	Ω
Load-side capacitor	C_{dc}	10	μ F
Grid-side capacitor	C_{ac}	2.8	μ F
Dead time	T_{d}	540	ns

FBDMC-SS WPT system. All other topologies are implemented on the same platform with minor modifications, for example, custom-made transformers, shown in the upper part of the figure, are used. Therefore, only the single FBDMC configuration is illustrated here. It should be noted that the modulation board is included in the center of the figure for illustration purposes only; in actual operation, it is isolated from the power circuit. As shown in Fig. 7, the FBDMC is designed as a modular converter composed of two half-bridge direct matrix converters (HBDMCs), which further enhances the modularity of the prototype. The performance of the FBDMC, the HBDMC, the two-HBDMC-based IPOS structure, and the two-HBDMC-based ISOP structure are evaluated and discussed in the following sections.

First of all, the parameters of the platforms are given in Table VI.

A. FBDMC

The output voltage and current waveforms are shown in Fig. 8. As can be seen from Fig. 8, the output voltage exhibits the 100-Hz envelope with the switching-frequency harmonics effectively suppressed. According to [42], pulse charging

Authorized licensed use limited to: TU Delft Library. Downloaded on October 06,2026 at 11:01:11 UTC from IEEE Xplore. Restrictions apply.

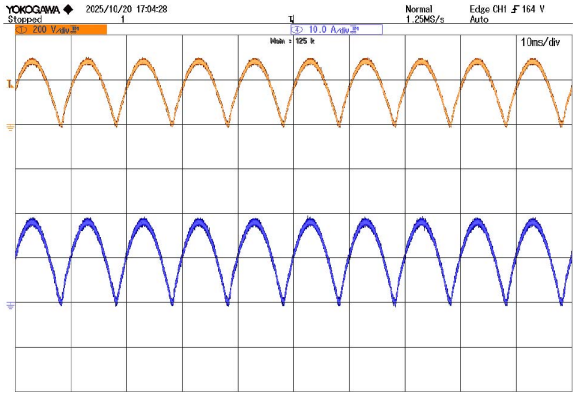


Fig. 8. The output waveforms of an FBDMC. The top orange waveform is the output voltage at the load. The bottom blue waveform is the output current at the load.

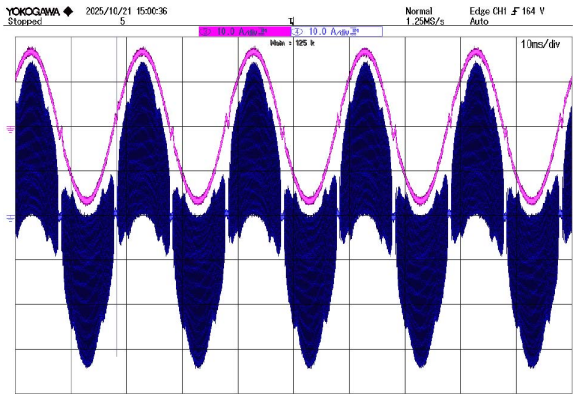


Fig. 9. The grid-side currents before and after the filter inductor. The top pink waveform is the grid current. The bottom blue waveform represents the current before the filter network.

remains effective for lithium-ion batteries and even offers advantages such as reduced maximum temperature rise. Based on the measured waveforms, the RMS value of the output voltage is 197.7 V, the RMS value of the output current is 12.7 A, resulting in an output power of 2510.8 W, while the grid input active power is measured as 2741 W, resulting in a grid-to-load efficiency of 91.6 %.

The grid-side currents before and after the filter inductor are illustrated in Fig. 9. The grid filter introduces a reactive power of 332 var, leading to a power factor (PF) of 0.992. Furthermore, the grid filter effectively suppresses the switching harmonics, and the total harmonic distortion (THD) of the grid current is reduced to 3.26 %.

The gate-source voltage of S_5 and i_p are shown in Fig. 10.

It can be observed that zero-voltage switching (ZVS) is achieved. However, around the grid-voltage zero-crossing point, the current magnitude is insufficient to provide the necessary reverse current, resulting in partial ZVS. Nevertheless, the corresponding switching losses are negligible due to the low voltage and current during this period. Fig. 11 shows a portion of the voltage and current waveforms of the resonant network, corresponding to several switching cycles. The complete 50-Hz period is not displayed, as the oscilloscope can only capture a limited time window without distortion. The captured

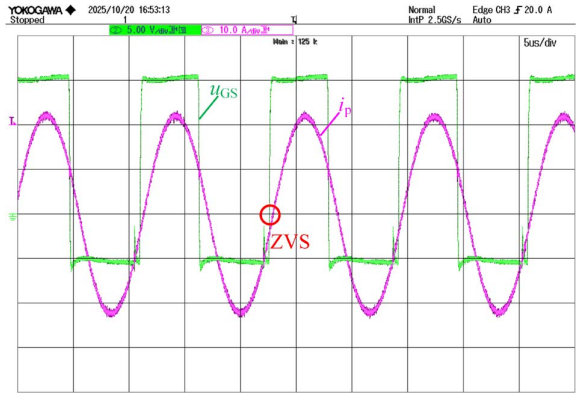


Fig. 10. The gate-source voltage of S_5 and the current of i_p.

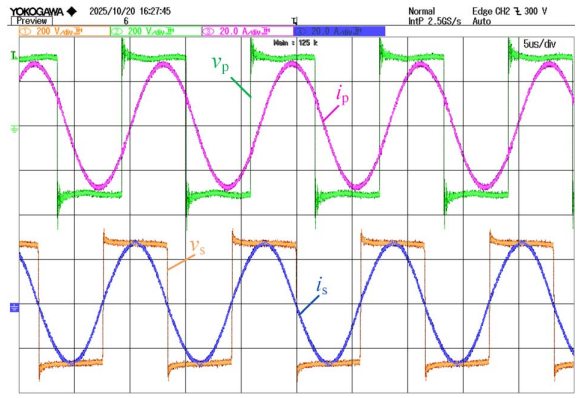


Fig. 11. A portion of the waveforms of v_p, v_s, i_p, i_s in the FBDMC system.

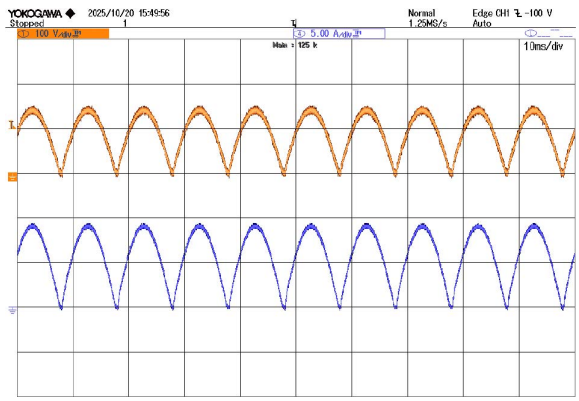


Fig. 12. The output waveforms of an HBDMC. The top orange waveform is the output voltage at the load. The bottom blue waveform is the output current at the load.

waveforms confirm that the network operates in a slightly inductive region, thereby ensuring ZVS operation.

B. HBDMC

An HBDMC is also tested using the same experimental platform. In this configuration, one bridge was removed, and a midpoint was drawn from the center of C_{ac} to connect the primary resonant network. The output voltage and current waveforms are shown in Fig. 12.

Based on the experimental data and calculations, the RMS values of the output voltage and current are 100.2 V and 6.4 A,

Authorized licensed use limited to: TU Delft Library. Downloaded on October 06,2026 at 11:01:11 UTC from IEEE Xplore. Restrictions apply.

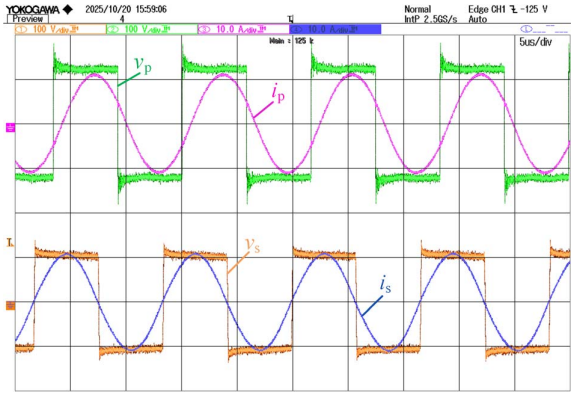


Fig. 13. A portion of the waveforms of v_p, v_s, i_p, i_s in the HBDMC system.

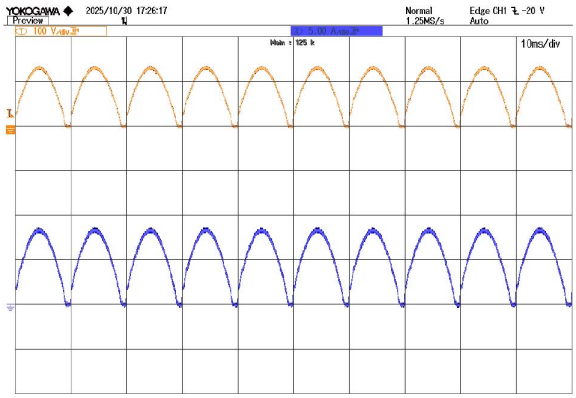


Fig. 14. The voltage and current waveforms on the load of the IPOS system. The top orange waveform is the output voltage at the load. The bottom blue waveform is the output current at the load.

respectively, corresponding to an output power of 641.3 W. The measured grid input power is 718 W, resulting in a grid-to-load efficiency of 89.3 %.

The voltage and current of the resonant network are shown in Fig. 13. It can be observed that the current is slightly inductive, thereby enabling ZVS operation.

C. IPOS

The modular IPOS and ISOP structures are implemented using two single HBDMCs. Regarding the IPOS structure, the grid voltage is set as 115 V to make the comparison with the single HBDMC with an input grid voltage of 230 V. Self-made high-coupling transformers are employed to provide galvanic isolation. The output voltage and current waveforms are shown in Fig. 14.

Based on the measured data, the RMS values of the output voltage and current are 91.2 V and 5.81 A, respectively, corresponding to an output power of 613 W. The measured grid input power is 530 W, resulting in a grid-to-load efficiency of 86.5 %. It can be observed from Table VII that the IPOS configuration maintains nearly the same output voltage and output current as the HBDMC system, even though it operates with only half of the input voltage. The difference between the HBDMC and IPOS mainly arises because the transformer is a self-made

TABLE VII
SUMMARY OF THE EXPERIMENTAL RESULTS. TOPO. MEANS THE TOPOLOGY. I.V. MEANS INPUT VOLTAGE. O.V. MEANS THE OUTPUT VOLTAGE. O.C. MEANS THE OUTPUT CURRENT. O.P. MEANS THE OUTPUT POWER. EFF. MEANS THE GRID-TO-LOAD EFFICIENCY

Topo.	I.V. (V)	O.V. (V)	O.C. (A)	O.P. (W)	Eff. (%)
FBDMC	230	197.7	12.7	2510.8	91.6
HBDMC	230	100.2	6.4	641.3	89.3
IPOS	115	91.2	5.81	530	86.5
ISOP	230	47.5	3.1	174	84.7

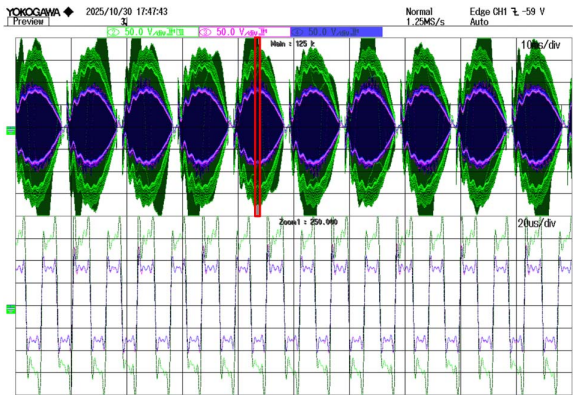


Fig. 15. The voltage waveforms of the two primary sides and the series-connected secondary side of the transformer of the IPOS system.

component rather than a carefully designed and optimized component, which leads to additional parasitic parameters, low power transfer capability, and efficiency. However, the design of a high-efficiency transformer is out of scope of this paper.

The voltage waveforms of the two primary sides and the series-connected secondary side of the transformer are shown in Fig. 15.

As shown in Fig. 15, the series connection of the two secondary windings enables voltage stacking in the IPOS configuration, resulting in an approximately doubled output voltage at the secondary side of the transformers.

D. ISOP

Regarding the ISOP configuration, the voltage and current waveforms on the load are shown in Fig. 16. Based on the measured data, the RMS values of the output voltage and current are 47.5 V and 3.1 A, corresponding to an output power of 147.3 W. The measured grid input power is 174 W, resulting in a grid-to-load efficiency of 84.7 %. The relatively low output performance results from the use of the half-bridge configuration and the limitation of the grid voltage, which was restricted to 230 V in the laboratory due to safety and equipment constraints. It should be emphasized that the purpose of this experiment is to verify the feasibility of the proposed ISOP configuration rather than to optimize the output performance.

The ISOP structure are proposed to share the voltage stress and the current stress of the semiconductor switches in each module. The current waveforms of each module and primary resonant network are shown in Fig. 17. It is clear from the figure

Authorized licensed use limited to: TU Delft Library. Downloaded on October 06,2026 at 11:01:11 UTC from IEEE Xplore. Restrictions apply.

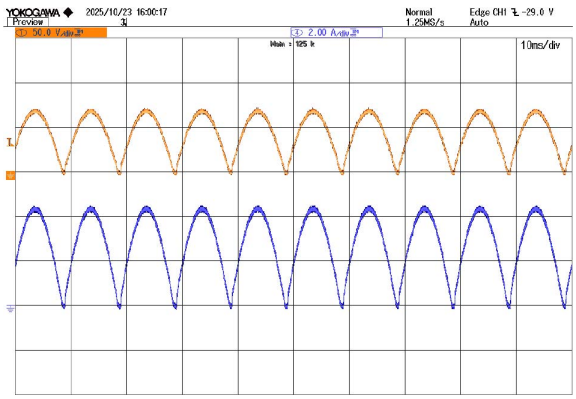


Fig. 16. The output voltage and current waveforms of the ISOP system. The top orange waveform is the output voltage at the load. The bottom blue waveform is the output current at the load.

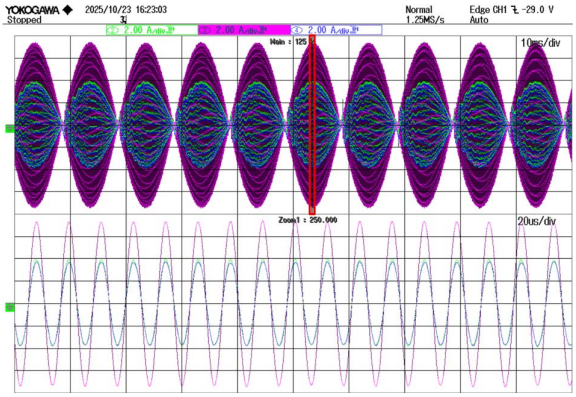


Fig. 17. The current waveforms of each module and primary resonant network of the ISOP system.

that ISOP structure can reduce the current stress of each module at the same load condition, proved the theory conclusion in Table IV.

E. Summary

All the experimental results are summarized in Table VII for clarity.

V. Conclusion

This paper proposes novel FBDMC-based high-power wireless charging systems. By eliminating the bulky DC-link capacitors through a direct AC-AC conversion approach, the proposed topology achieves higher power density and improved reliability compared to the conventional WPT systems based on two-stage primary power conversion. The single AC-FBDMC-SS WPT system is analyzed and experimentally validated, showing equivalent performance to the conventional DC-FBI-SS WPT system.

Although several WPT charging systems based on single-stage front-end converters have been reported in [30], [31], [32], [33], [34], [35], [36], [37], [38], most of these designs employ non-scalable circuit structures or indirect matrix converters, which hinder system modularization and lead to lower power density compared with DMCs. Only the work in [37] adopts a similar bidirectional-switch-based DMC topology, featuring a three-phase input with an input voltage of 150 VAC, and achieving an output power of approximately 2.2 kW with an efficiency of about 87 %. In contrast, the proposed FBDMC-based WPT system achieves an output power of 2.51 kW with a grid-to-load efficiency of 91.6 % at an input voltage of 230 VAC.

Two modular configurations, namely IPOS and ISOP, are introduced to address low-voltage and MVAC grid applications, respectively. The IPOS configuration connects multiple converters in parallel on the input side and in series on the output side, enabling higher output voltage and improved efficiency under limited input-voltage conditions. It is particularly suitable for medium-power wireless charging systems such as residential applications. In contrast, the ISOP configuration connects modules in series on the input side and in parallel on the output side, providing superior scalability for high-power and MVAC grid integration. Simulation and experimental results verified its capability to share voltage and current stresses among modules, demonstrating potential for MW-level charging with commercial semiconductor switches. Future work will focus on developing advanced modulation and control strategies to enable dual-side control and bidirectional power flow in the proposed modular DMC-based WPT systems.

References

[1] "Lorries, buses and coaches," European Commission, 2026. Accessed on: Jan. 29, 2026. [Online]. Available: https://climate.ec.europa.eu/eu-action/transport-decarbonisation/road-transport/lorries-buses-and-coaches_en

[2] E. Mulholland, "The revised CO2 standards for heavy-duty vehicles in the European Union," Int. Council on Clean Transp. (ICCT), Tech. Rep., May 2024. Accessed on: Jan. 29, 2026. [Online]. Available: https://www.theicct.org/publication/europe-heavy-duty-vehicle-co2-standards-may23/

[3] E. Rock Drills AB, "Minetruck MT42 battery: Technical Specifications," Epiroc Rock Drills AB, Örebro, Sweden, Tech. Rep. 9869 0138 01g, 2022.

[4] S. Mining and R. Technology, "Sandvik TH550B battery-electric underground truck," 2026. Accessed on Jan. 29, 2026. [Online]. Available: https://www.mining.sandvik/en/products/equipment/trucks/th550b/

[5] J. H. Kim et al., "Development of 1-mw inductive power transfer system for a high-speed train," *IEEE Trans. Ind. Electron.*, vol. 62, pp. 6242–6250, Oct. 2015.

[6] J. Lee, M.-Y. Kim, and S.-H. Lee, "Design methodology for a transformerless multilevel inductive power transfer system," in *Proc. IEEE Energy Convers. Congr. Expo. (ECCE)*, 2021, pp. 1640–1647.

[7] J. Lee, M.-Y. Kim, and S.-H. Lee, "Novel transformerless multilevel inductive power transfer system," *IEEE Access*, vol. 10, pp. 55565–55573, 2022.

[8] J. Lee and S.-H. Lee, "Analysis and design of load-independent, efficient, transformerless multilevel online inductive power transfer system," *IEEE Trans. Ind. Electron.*, vol. 71, pp. 10455–10464, Sep. 2024.

[9] G. Guidi, J. A. Suul, F. Jenset, and I. Sorfonn, "Wireless charging for ships: High-power inductive charging for battery electric and plug-in hybrid vessels," *IEEE Electrific. Mag.*, vol. 5, pp. 22–32, Sep. 2017.

[10] B. X. Nguyen, D. M. Vilathgamuwa, G. Foo, P. Wang, and A. Ong, "A modified cascaded multilevel converter topology for high power bidirectional inductive power transfer systems with the reduction of switching devices and power losses," in *Proc. IEEE 11th Int. Conf. Power Electron. Drive Syst.*, 2015, pp. 93–97.

[11] S. Wang and D. Dorrell, "Simulation of electric vehicle inductive charging systems," in *Proc. IEEE 11th Int. Conf. Power Electron. Drive Syst.*, 2015, pp. 399–404.

[12] B. X. Nguyen, W. Peng, and D. M. Vilathgamuwa, "Multilevel converter topologies based high power inductive power transfer systems," in *Proc. IEEE Int. Conf. Sustain. Energy Technol. (ICSET)*, 2016, pp. 264–269.

Authorized licensed use limited to: TU Delft Library. Downloaded on October 06,2026 at 11:01:11 UTC from IEEE Xplore. Restrictions apply.

[13] P. Briceño, A. Watson, J. Clare, P. Wheeler, P. Venugopal, and T. B. Soeiro, "Optimizing wireless power transfer efficiency in cascaded h-bridge converter through an auxiliary resonant circuit pole," in *Proc. IECON – 49th Annu. Conf. IEEE Ind. Electron. Soc.*, 2023, pp. 1–8.
[14] W. V. Wang, D. J. Thirmawithana, B. Riar, and R. Zane, "A novel integrated boost modular multilevel converter for high power wireless EV charging," in *Proc. IEEE Energy Convers. Congr. Expo. (ECCE),* 2018, pp. 81–88.
[15] W. V. Wang and D. J. Thrimawithana, "A novel converter topology for a primary-side controlled wireless EV charger with a wide operation range," *IEEE J. Emerg. Sel. Topics Ind. Electron.*, vol. 1, pp. 36–45, Jul. 2020.
[16] W. V. Wang, F. J. Lin, D. J. Thirmawithana, and G. Covic, "A modular multilevel converter based inductive power transfer system," in *Proc. IEEE Energy Convers. Congr. Expo. (ECCE),* 2021, pp. 5761–5766.
[17] W. V. Wang, D. J. Thrimawithana, F. Lin, and G. A. Covic, "An mmc-based IPT system with integrated magnetics and ZVS operations," *IEEE Trans. Power Electron.*, vol. 37, pp. 2425–2436, Feb. 2022.
[18] W. V. Wang, D. J. Thrimawithana, and M. Neuburger, "An Si MOSFET-based high-power wireless EV charger with a wide ZVS operating range," *IEEE Trans. Power Electron.*, vol. 36, pp. 11163–11173, Oct. 2021.
[19] J. Kumar, S. Sharma, and S. K. Patro, "Derived modular multilevel converter for EV charging stations," in *Proc. 7th Int. Conf. Comput. Appl. Electr. Eng. – Recent Adv. (CERA)*, 2023, pp. 1–6.
[20] Q. Deng, J. Liu, D. Czarkowski, W. Hu, and H. Zhou, "An inductive power transfer system supplied by a multiphase parallel inverter," *IEEE Trans. Ind. Electron.*, vol. 64, pp. 7039–7048, Sep. 2017.
[21] Q. Deng, P. Sun, W. Hu, D. Czarkowski, M. K. Kazimierczuk, and H. Zhou, "Modular parallel multi-inverter system for high-power inductive power transfer," *IEEE Trans. Power Electron.*, vol. 34, pp. 9422–9434, Oct. 2019.
[22] Q. Deng et al., "Modeling and control of inductive power transfer system supplied by multiphase phase-controlled inverter," *IEEE Trans. Power Electron.*, vol. 34, no. 9, pp. 9303–9315, Sep. 2019.
[23] A. Zhu et al., "Modeling and phase synchronization control of high-power wireless power transfer system supplied by modular parallel multi-inverters," *IEEE Trans. Veh. Technol.*, vol. 70, no. 9, pp. 6450–6462, Jul. 2021.
[24] E. Ayaz, O. Altun, H. Polat, and O. Keysan, "Generalized model of modular two element compensated IPT systems with common dc-bus," in *Proc. Wireless Power Week (WPW),* 2022, pp. 260–265.
[25] X. Liu et al., "A multi-inverter high-power wireless power transfer system with wide ZVS operation range," *IEEE Trans. Power Electron.*, vol. 37, no. 12, pp. 14082–14095, Dec. 2022.
[26] Y. Wang, S. Zhao, R. Kheirollahi, A. Mostafa, H. Zhang, and F. Lu, "Multiphase interleaved IPT based current-source converter for high-current application," *IEEE J. Emerg. Sel. Topics Ind. Electron.*, vol. 3, no. 3, pp. 583–593, Jul. 2022.
[27] H. Hu, J. Su, F. Chen, and Y. Sun, "Modularized inductive power transfer systems with inherent impedance decoupling for high-power applications," *IEEE Trans. Ind. Electron.*, vol. 71, no. 2, pp. 1492–1502, Feb. 2024.
[28] X. Li, D. Zhou, S. Jia, X. Liu, and J. Zou, "A WPT system with wide-range voltage gains and soft switching via primary-side hybrid modulation," *IEEE Trans. Power Electron.*, vol. 39, no. 7, pp. 8985–8997, Jul. 2024.
[29] D. B. Yelaverthi, R. Hatch, M. Mansour, H. Wang, and R. Zane, "3-level asymmetric full-bridge soft-switched PWM converter for 3-phase unfolding based battery charger topology," in *Proc. IEEE Energy Convers. Congr. Expo. (ECCE),* 2019, pp. 2737–2743.
[30] E. Asa et al., "A novel ac-to-ac wireless power transfer system for EV charging applications," in *Proc. IEEE Appl. Power Electron. Conf. Expo. (APEC),* 2020, pp. 1685–1690.
[31] C. R. Teeneti, R. Hatch, D. B. Yelaverthi, A. Kamineni, H. Wang, and R. Zane, "Unfolder-based single-stage AC-AC conversion system for wireless charging applications," in *Proc. IEEE Energy Convers. Congr. Expo. (ECCE),* 2020, pp. 5193–5198.
[32] M. Dabkara, A. Jakhar, and A. K. Verma, "A dual clamped AC-AC converter based inductive charging system," in *Proc. IEEE Transp. Electrific. Conf. (ITEC-India),* 2021, pp. 1–6.
[33] J. Liu, C. S. Wong, Z. Li, X. Jiang, and K. Loo, "An integrated three-phase AC–DC wireless-power-transfer converter with active power factor correction using three transmitter coils," *IEEE Trans. Power Electron.*, vol. 38, no. 6, pp. 7821–7835, Jun. 2023.
[34] X. Zhang, Q. Zhang, and F. Zhang, "Triple phase ratio shift control for bidirectional wireless power transfer application based on totem-pole single-stage AC-AC converter," *IEEE Trans. Power Electron.*, vol. 40, no. 8, pp. 11863–11873, Aug. 2025.
[35] G. Dong, T. Mishima, H. Omori, and C.-M. Lai, "A single-phase direct AC-AC wireless power transfer system using conduction mode-exchanged pulse density modulation," in *Proc. IEEE Transp. Electrific. Conf. Expo, Asia-Pacific (ITEC Asia-Pacific),* 2023, pp. 1–5.
[36] E. Asa et al., "A 20-kW DC oak ridge converter with integrated ac and dc sources for grid services and energy storage systems," in *Proc. IEEE Appl. Power Electron. Conf. Expo. (APEC),* 2022, pp. 464–468.
[37] Y. Xiao and C. Liu, "Direct load voltage control for electrolytic capacitorless wireless power transfer system without dc/dc converter," *IEEE Trans. Ind. Electron.*, vol. 68, no. 9, pp. 8039–8048, Sep. 2021.
[38] A. Zade et al., "A 21-kW unfolding-based single-stage Ac–Dc converter for wireless charging applications," *IEEE Trans. Emerg. Sel. Topics Power Electron.*, vol. 12, no. 1, pp. 8–22, Feb. 2024.
[39] TDK Electronics AG, "Aluminum electrolytic capacitors with screw terminals: Series b43700 and b43720," TDK Electronics AG, Munich, Germany, Tech. Rep., Dec. 2019. Available: https://www.tdk-electronics.tdk.com/inf/20/30/db/aec/B43700_B43720.pdf
[40] F. T. Jauch, "Medium voltage AC-DC converter systems for ultra-fast charging stations for electric vehicles," Ph.D. thesis, ETH Zurich, Zurich, Switzerland, 2016.
[41] R. L. Steigerwald, "A comparison of half-bridge resonant converter topologies," *IEEE Trans. Power Electron.*, vol. 3, no. 2, pp. 174–182, Apr. 1988.
[42] X. Huang, W. Liu, A. B. Acharya, J. Meng, R. Teodorescu, and D.-I. Stroe, "Effect of pulsed current on charging performance of lithium-ion batteries," *IEEE Trans. Ind. Electron.*, vol. 69, pp. 10144–10153, Oct. 2022.
[43] W. Shi et al., "Design of a highly efficient 20-kw inductive power transfer system with improved misalignment performance," *IEEE Trans. Transport. Electrific.*, vol. 8, no. 2, pp. 2384–2399, Jun. 2022.
[44] R. Bosshard, J. W. Kolar, J. Mühlethaler, I. Stevanović, B. Wunsch, and F. Canales, "Modeling and η-α-pareto optimization of inductive power transfer coils for electric vehicles," *IEEE Trans. Emerg. Sel. Topics Power Electron.*, vol. 3, no. 1, pp. 50–64, Mar. 2015.
[45] Z. Li, E. Hsieh, Q. Li, and F. C. Lee, "High-frequency transformer design with medium-voltage insulation for resonant converter in solid-state transformer," *IEEE Trans. Power Electron.*, vol. 38, no. 8, pp. 9917–9932, Aug. 2023.
[46] R. Bosshard and J. W. Kolar, "Multi-objective optimization of 50 kW/85 kHz IPT system for public transport," *IEEE Trans. Emerg. Sel. Topics Power Electron.*, vol. 4, no. 4, pp. 1370–1382, Dec. 2016.
[47] SAE, "Wireless power transfer for heavy-duty electric vehicles," SAE, Warrendale, PA, USA, SAE J2954/2, Dec. 2022.

Authorized licensed use limited to: TU Delft Library. Downloaded on October 06,2026 at 11:01:11 UTC from IEEE Xplore. Restrictions apply.